



Investigating the Atmospheric Mass Loss of the Kepler-105 Planets Straddling the Radius Gap

Aaron Householder^{1,2,23} , Lauren M. Weiss³ , James E. Owen⁴ , Howard Isaacson^{5,6} , Andrew W. Howard⁷ , Daniel Fabrycky⁸ , Leslie A. Rogers⁹ , Hilke E. Schlichting¹⁰ , Benjamin J. Fulton^{11,12} , Erik A. Petigura¹³ , Steven Giacalone^{5,7} , Joseph M. Akana Murphy^{14,24} , Corey Beard^{15,25} , Ashley Chontos^{16,17} , Fei Dai^{7,18,26} , Judah Van Zandt¹³ , Jack Lubin¹⁹ , Malena Rice² , Alex S. Polanski²⁰ , Paul Dalba²¹ , Sarah Blunt⁷ , Emma V. Turtelboom²² , Ryan Rubenzahl^{7,27} , and Casey Brinkman¹⁷ 

¹ Department of Earth, Atmospheric and Planetary Sciences, Massachusetts Institute of Technology, Cambridge, MA 02139, USA; aaron593@mit.edu

² Department of Astronomy, Yale University, 52 Hillhouse, New Haven, CT 06511, USA

³ Department of Physics and Astronomy, University of Notre Dame, Notre Dame, IN 46556, USA

⁴ Astrophysics Group, Department of Physics, Imperial College London, Prince Consort Road, London SW7 2AZ, UK

⁵ Department of Astronomy, University of California Berkeley, Berkeley, CA 94720, USA

⁶ Centre for Astrophysics, University of Southern Queensland, Toowoomba, QLD, Australia

⁷ Department of Astronomy, California Institute of Technology, Pasadena, CA 91125, USA

⁸ Dept. of Astronomy & Astrophysics, University of Chicago, 5640 S. Ellis Avenue, Chicago, IL 60637, USA

⁹ Department of Astronomy and Astrophysics, University of Chicago, Chicago, IL 60637, USA

¹⁰ Department of Earth, Planetary, and Space Sciences, The University of California, Los Angeles, 595 Charles E. Young Drive East, Los Angeles, CA 90095, USA

¹¹ Cahill Center for Astronomy & Astrophysics, California Institute of Technology, Pasadena, CA 91125, USA

¹² IPAC-NASA Exoplanet Science Institute, Pasadena, CA 91125, USA

¹³ Department of Physics & Astronomy, University of California Los Angeles, Los Angeles, CA 90095, USA

¹⁴ Department of Astronomy and Astrophysics, University of California, Santa Cruz, CA 95064, USA

¹⁵ Department of Physics & Astronomy, The University of California, Irvine, Irvine, CA 92697, USA

¹⁶ Department of Astrophysical Sciences, Princeton University, 4 Ivy Lane, Princeton, NJ 08540, USA

¹⁷ Institute for Astronomy, University of Hawaii, 2680 Woodlawn Drive, Honolulu, HI 96822 USA

¹⁸ Division of Geological and Planetary Sciences, 1200 E California Boulevard, Pasadena, CA, 91125, USA

¹⁹ Department of Physics & Astronomy, University of California Irvine, Irvine, CA 92697, USA

²⁰ Department of Physics and Astronomy, University of Kansas, Lawrence, KS 66045, USA

²¹ Department of Earth & Planetary Sciences, University of California Riverside, 900 University Avenue, Riverside, CA 92521, USA

²² Department of Astronomy, 501 Campbell Hall, University of California, Berkeley, CA 94720, USA

Received 2023 September 20; revised 2023 December 3; accepted 2023 December 5; published 2024 January 31

Abstract

An intriguing pattern among exoplanets is the lack of detected planets between approximately $1.5 R_{\oplus}$ and $2.0 R_{\oplus}$. One proposed explanation for this “radius gap” is the photoevaporation of planetary atmospheres, a theory that can be tested by studying individual planetary systems. Kepler-105 is an ideal system for such testing due to the ordering and sizes of its planets. Kepler-105 is a Sun-like star that hosts two planets straddling the radius gap in a rare architecture with the larger planet closer to the host star ($R_b = 2.53 \pm 0.07 R_{\oplus}$, $P_b = 5.41$ days, $R_c = 1.44 \pm 0.04 R_{\oplus}$, $P_c = 7.13$ days). If photoevaporation sculpted the atmospheres of these planets, then Kepler-105b would need to be much more massive than Kepler-105c to retain its atmosphere, given its closer proximity to the host star. To test this hypothesis, we simultaneously analyzed radial velocities and transit-timing variations of the Kepler-105 system, measuring disparate masses of $M_b = 10.8 \pm 2.3 M_{\oplus}$ ($\rho_b = 3.68 \pm 0.84 \text{ g cm}^{-3}$) and $M_c = 5.6 \pm 1.2 M_{\oplus}$ ($\rho_c = 10.4 \pm 2.39 \text{ g cm}^{-3}$). Based on these masses, the difference in gas envelope content of the Kepler-105 planets could be entirely due to photoevaporation (in 76% of scenarios), although other mechanisms like core-powered mass loss could have played a role for some planet albedos.

Unified Astronomy Thesaurus concepts: [Exoplanet atmospheres \(487\)](#); [Exoplanet formation \(492\)](#); [Exoplanet evolution \(491\)](#); [Radial velocity \(1332\)](#); [Transit timing variation method \(1710\)](#); [Exoplanets \(498\)](#)

Supporting material: machine-readable table

1. Introduction

In one of the most significant exoplanet discoveries in recent years, Fulton et al. (2017) identified a gap in the occurrence rate of exoplanets between approximately $1.5 R_{\oplus}$ and $2.0 R_{\oplus}$. Various theories have been proposed to explain this “radius gap,” two of which are particularly prominent: core-powered mass loss (Ginzburg et al. 2018; Gupta & Schlichting 2019) and photoevaporation (Owen & Wu 2017). As planets form and accrete gas and dust from the protoplanetary disk, they can become surrounded by a gaseous envelope. However, this primordial envelope can be removed. Core-powered mass-loss facilitates the loss of planetary atmospheres due to the cooling

²³ MIT Dean of Science Fellow.

²⁴ NSF Graduate Research Fellow.

²⁵ NASA FINESST Fellow.

²⁶ NASA Sagan Fellow.

²⁷ NSF Graduate Research Fellow.



luminosity of a planet’s core. X-ray and ultraviolet (XUV) radiation from the host star can also drive atmospheric mass loss via photoevaporation, where the XUV radiation ionizes and heats up the gas in the planetary atmosphere, causing it to escape into space. Both of these processes can cause planets to lose a substantial amount of their gas envelopes, leading to a significant reduction in their overall radii. Theoretical models suggest that planets within the radius gap ($1.5 R_{\oplus}$ – $2.0 R_{\oplus}$) lose their gas envelopes on short timescales, leading to a reduction in their radii, whereas planets larger than the gap have much longer timescales for atmospheric mass loss (Lopez & Fortney 2013; Owen & Wu 2013, 2017; Mordasini 2020). Furthermore, planets smaller than $1.5 R_{\oplus}$ that are close to their stars are typically thought to be rocky, in which case they have no atmospheres left to lose (Weiss & Marcy 2014; Rogers 2015).

The explanation of the radius gap is sometimes framed as a binary choice between core-powered mass loss and photoevaporation. However, such a simplistic interpretation likely does not encompass the full complexity of atmospheric mass loss for the planets in this regime. A more nuanced approach to understanding the radius gap likely involves a combination of both core-powered mass loss and photoevaporation, each playing a role in sculpting planetary architectures. Therefore, instead of seeking a definitive answer to which theory explains the radius gap, it is more prudent to explore how each mechanism contributes to shaping different types of planetary architectures. Studying individual planetary systems offers a unique advantage in this context. By focusing on planets that share the same host star properties (i.e., mass, radius, temperature, age, XUV radiation history, and metallicity), we can eliminate a multitude of confounding factors that limit broader population studies. Thus, individual planetary systems provide us with a more robust testbed for examining theories such as photoevaporation and core-powered mass loss.

Kepler-105 is a system that serves as an excellent natural laboratory for investigating the role of photoevaporation in sculpting planetary architectures. In the case of photoevaporation-driven atmospheric mass loss, the time-integrated XUV radiation that a planet receives affects how much atmosphere the planet loses. Thus, the best systems for testing photoevaporation have an unusual architecture in which a gas-rich sub-Neptune is interior to a rocky planet (Owen & Campos Estrada 2020a). Kepler-105 has two confirmed planets that follow this architecture: a sub-Neptune ($R_b = 2.53 \pm 0.07 R_{\oplus}$) with a period of 5.41 days and a super-Earth ($R_c = 1.44 \pm 0.04 R_{\oplus}$) with a period of 7.13 days (Fulton & Petigura 2018). Based on previous mass measurements of planets with similar sizes, we expect Kepler-105c to have a predominantly rocky composition, while Kepler-105b likely has a significant gaseous envelope. If their compositions are typical for their sizes, it is unclear how the inner planet, which likely received more XUV flux from the host star, managed to retain a significant gaseous envelope while the smaller outer planet did not.

A similar problem was posed for Kepler-36, a benchmark system that played an important role in developing radius valley predictions and photoevaporation models (Carter et al. 2012; Lopez & Fortney 2013; Owen & Campos Estrada 2020a). Kepler-36 hosts two confirmed planets near the 6:7 mean-motion resonance (MMR), with a Neptune-sized planet exterior to a super-Earth. The Neptune-sized planet was found to possess a much more massive core, thereby making it more likely to retain a gaseous envelope (Lopez & Fortney 2013). These findings

prompted us to explore a similar scenario for the Kepler-105 system. If Kepler-105b and Kepler-105c formed in situ, then Kepler-105b would receive $\sim 44\%$ more cumulative XUV radiation than Kepler-105c. Thus, similar to the Kepler-36 system, the mass of Kepler-105b must be substantially larger than that of Kepler-105c for the latter to have lost its envelope due to photoevaporation while the former retained it.

To test this hypothesis, we first analyzed transit-timing variations (TTVs; Section 2) and radial velocities (RVs; Section 3) to measure the masses of both planets. We then jointly modeled the TTVs and RVs to refine these mass measurements in Section 4 and explored potential planetary compositions (Section 5). Section 6 compares our measured masses with numerical predictions from `EvapMass` (Owen & Campos Estrada 2020b). This allows us to assess the viability of photoevaporation to explain the observed difference in gas content between Kepler-105b and Kepler-105c. We also explore core-powered mass loss as an alternative mechanism to explain the different gas compositions of these planets. Finally, in Section 7, we provide a summary of our findings and outline potential avenues for future research related to Kepler-105.

2. Mass From TTVs

TTVs are variations in the orbital period of a planet caused by the gravitational influence of other objects in the same system such as planets or moons. Since the amplitude of the TTV of a planet depends on the mass of the companion (Lithwick et al. 2012), we can use TTVs to measure the masses of Kepler-105b and Kepler-105c, which are interior to the 4:3 MMR (Fulton & Petigura 2018). We analyzed 246 transit times for Kepler-105b and 179 transit times for Kepler-105c from Q1 to Q17 short and long cadence data from the Kepler Space Telescope (J. Rowe, 2022, private communication; based on Rowe et al. 2015), shown in Figure 1 with a linear ephemeris subtracted. To model the TTVs, we used `TTVFaster` (Agol & Deck 2016), which uses perturbation theory to model all terms to first-order in eccentricity. This semianalytic approach has been demonstrated to produce accurate results for planets that are low-mass, low-eccentricity and not too deep within resonance (Agol & Deck 2016), such as Kepler-105b and Kepler-105c. To find the best fit to the transit times of Kepler-105b and Kepler-105c using `TTVFaster`, we maximized the following log-likelihood function:

$$\log(\mathcal{L}) = -0.5 \sum_i \frac{(\text{TT}_i - \text{TT}_{m,i})^2}{\sigma_{\text{TT},i}^2} \quad (1)$$

where TT_i and $\text{TT}_{m,i}$ are the observed and model-predicted transit times for the i -th observation, respectively, and $\sigma_{\text{TT},i}$ is the observational uncertainty for that transit. \sum_i indicates that we sum over all observed transits for both Kepler-105b and Kepler-105c.

To explore various solutions in our parameter space we used `emcee` (Foreman-Mackey et al. 2013): a Python package that runs a Markov chain Monte Carlo (MCMC) algorithm with an affine-invariant ensemble sampler (Goodman & Weare 2010). We varied the masses (M), orbital periods (P), $\sqrt{e} \cos \omega_p$, $\sqrt{e} \sin \omega_p$, and the initial times of transit (t_0). We reparameterized e and ω in this way to mitigate against an artificial build up of eccentricities near zero due to the boundary condition at $e = 0$ (Eastman et al. 2013). We allowed stellar mass to vary as well,

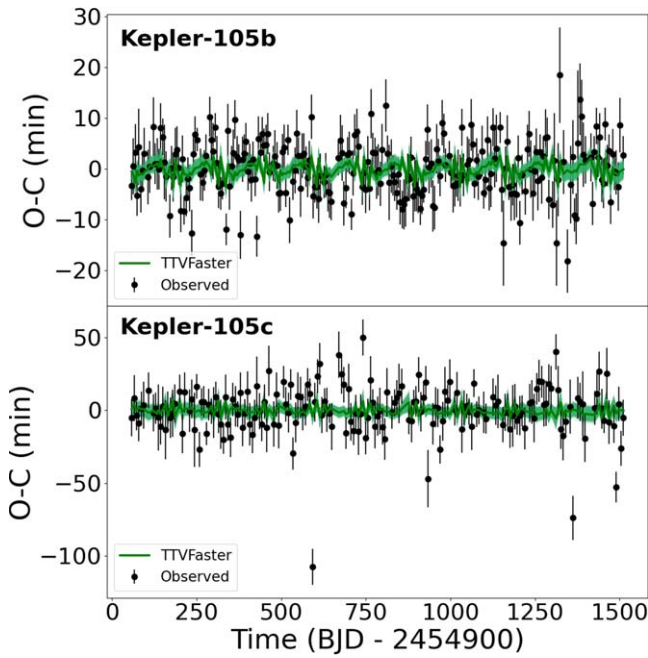


Figure 1. Observed transit times minus a linear ephemeris (black) for Kepler-105b (top) and Kepler-105c (bottom). The plot also includes the best fit *TTVFaster* (Agol & Deck 2016) solution to the TTVs (dark green) as well as the 1σ confidence intervals from our model (light green). Our TTV model is strongly preferred to a linear ephemeris ($\Delta AIC = -27$, where AIC is the Akaike information criterion; Akaike 1974), indicating the presence of dynamical perturbations affecting the transit times. Based on the TTVs alone, we detected Kepler-105c with 4σ confidence ($5.9 \pm 1.4 M_{\oplus}$) and Kepler-105b with 2σ confidence ($9.3^{+4.9}_{-4.6} M_{\oplus}$). Furthermore, we ran two additional MCMC runs where the mass of Kepler-105c was constrained to be either $\leq 3.1 M_{\oplus}$ or $\geq 8.7 M_{\oplus}$. Our best-fit *TTVFaster* analytic solution was strongly preferred over these MCMC models ($\Delta AIC = -11$ for both cases).

using a Gaussian prior of $0.99 \pm 0.03 M_{\odot}$ based on previous stellar characterization (Fulton & Petigura 2018). Since the planets in Kepler-105 have very close orbits, we used a Hill stability prior to prevent orbit crossing:

$$\begin{aligned}
 & a_c(1 - e_c) > a_b(1 + e_b) \\
 & + \max \left(a_b(1 - e_b) \left(\frac{M_b}{3M_*} \right)^{\frac{1}{3}} \right. \\
 & \left. a_c(1 - e_c) \left(\frac{M_c}{3M_*} \right)^{\frac{1}{3}} \right), \quad (2)
 \end{aligned}$$

where a represents the semimajor axes for Kepler-105b and Kepler-105c (denoted with subscripts b and c) and M_* represents the stellar mass. Gaussian priors were placed on P and t_0 and uniform priors were placed on e , ω and M (see Table 1). We determined a in Equation (2) using Kepler’s Third Law from P and M_* . We also fixed the orbital inclinations of the planets in an edge-on configuration ($i = 90^\circ$). This is because *TTVFaster* assumes coplanar orbits for each planet since the amplitude of TTVs scales with mutual inclination to second order (Lithwick et al. 2012). With this setup, we ran the MCMC until convergence, discarding the first 10^5 steps as burn-in. To check for convergence, we used the potential scale reduction factor (PSRF; Gelman & Rubin 1992), requiring each parameter in our model to have a PSRF less than 1.01.

Our MCMC analysis of the TTVs yielded a mass of $9.3^{+4.9}_{-4.6} M_{\oplus}$ for Kepler-105b and a mass of $5.9 \pm 1.4 M_{\oplus}$ for

Kepler-105c. These findings place strong constraints on the mass of Kepler-105c (4σ), but not Kepler-105b (only 2σ). This outcome is consistent with previous TTV analyses of the system (Hadden & Lithwick 2017; Jontof-Hutter et al. 2016). However, this may seem surprising, given that Kepler-105b is more massive and should theoretically induce larger and more easily detectable TTVs than Kepler-105c. The explanation for this is two-fold. First, the mass error for Kepler-105c scales with the transit midpoint error of the larger Kepler-105b. Second, Kepler-105b produces a deeper transit, making it easier to precisely measure the midpoint of each transit. Thus, the higher precision in transit midpoint measurements of Kepler-105b leads to better constraints on the mass of Kepler-105c. By the same logic, the mass of Kepler-105b is not as well determined from TTVs due to the smaller transit depth of Kepler-105c, which leads to larger transit midpoint uncertainties for Kepler-105c.

3. Mass From RVs

The RV method is a commonly used exoplanet detection technique that involves measuring the Doppler shift in the emitted light of a star caused by the gravitational influence of orbiting planets. In this paper, we measured 92 RV observations of Kepler-105 (Table 2) with the High Resolution Echelle Spectrometer (HIRES) on Keck I (Vogt et al. 1994). The observations of Kepler-105 were performed using the C2 Decker with typical exposure times of 1800 s (median S/N at $5500 \text{ \AA} = 89 \text{ pix}^{-1}$). The data was processed through the standard HIRES RV data reduction pipeline (Howard et al. 2010).

3.1. Simple Two-planet Model

Given the challenges in accurately deducing planetary properties from RV data, which is often complicated by the presence of stellar activity, we faced a decision on how to model the RVs. For instance, we could include a Gaussian process (GP) into our RV model to help model the correlated noise from stellar activity (e.g., Haywood et al. 2014; Grunblatt et al. 2015; Rajpaul et al. 2015). However, Kepler-105 is a low-activity star ($\log R'_{\text{HK}} = -5.19$), so incorporating a correlated noise model may introduce unnecessary free parameters (e.g., Blunt et al. 2023). Thus, we chose to model the RVs twice, both with and without a GP, to determine which model produced a more reliable fit to the data. For our first approach, we implemented a simple two-planet Keplerian model using the Radial Velocity Modeling Toolkit *RadVel* (Fulton et al. 2018). We allowed P , $\sqrt{e} \cos \omega_*$, $\sqrt{e} \sin \omega_*$, t_0 and the RV semi-amplitude (K) to vary for both Kepler-105b and Kepler-105c. Similar to our TTV model, we used Gaussian priors on P and t_0 and uniform priors on e , ω , and K (Table 1). Additionally, we include two nuisance parameters, jitter (σ_{jit}) and gamma (γ), to account for additional astronomical and instrumental noise and the RV offset, respectively. Lastly, we used a Hill stability prior to prevent orbit crossing (Equation (2)).

3.2. GP Model

We also extended the simple two-planet model in 3.1 by including a GP to model correlated noise in the RVs caused by stellar activity. To fully specify a GP, one must define a covariance function, often referred to as a “kernel” (Rasmussen & Williams 2006). Given the quasi-periodic nature of stellar

Table 1

Dynamical Parameters of Kepler-105b and Kepler-105c from an RV-only Fit (RadVel), a TTV-only Fit (TTVFaster), and a Simultaneous Fit to RVs and TTVs (RadVel and TTVFaster)

Parameter	RV-only	TTV-only	Joint RV and TTV	Prior
P_b (days)	5.412207 ± 0.000002	5.41220324 ± 0.0000003	5.4122034 ± 0.0000004	Norm (5.412207130, 0.000002488)
e_b	0.05 ± 0.04	0.01 ± 0.01	0.02 ± 0.02	Unif (0, 1)
ω_b ($^\circ$)	$358.6^{+92.8}_{-159.0}$	$61.2^{+60.0}_{-142.5}$	$225.0^{+68.4}_{-137.1}$	Unif (0, 360)
$t_{0,b}$ (BJD)	2454955.3185 ± 0.0006	2454955.3186 ± 0.0003	2454955.3186 ± 0.0002	Norm (2454955.318609, 0.000536)
M_b (M_\oplus)	10.7 ± 2.8	$9.3^{+4.9}_{-4.6}$	10.8 ± 2.3	Unif (0, 50)
R_b (R_\oplus)	2.53 ± 0.07	2.53 ± 0.07	2.53 ± 0.07	...
ρ_b (g cm^{-3})	3.65 ± 1.01	$3.17^{+1.69}_{-1.59}$	3.68 ± 0.84	...
P_c (days)	7.12594 ± 0.00001	7.12592 ± 0.00001	7.12592 ± 0.00001	Norm (7.125945910, 0.000012500)
e_c	0.04 ± 0.04	0.02 ± 0.02	0.02 ± 0.02	Unif (0, 1)
ω_c ($^\circ$)	$310.9^{+156.4}_{-112.4}$	$124.3^{+156.1}_{-67.4}$	$298.9^{+135.7}_{-59.5}$	Unif (0, 360)
$t_{0,c}$ (BJD)	2454957.753 ± 0.0001	2454957.754 ± 0.0003	2454957.753 ± 0.0001	Norm (2454957.753432, 0.001687)
M_c (M_\oplus)	4.6(95% UpperLimit)	5.9 ± 1.4	5.6 ± 1.2	Unif (0, 50)
R_c (R_\oplus)	1.44 ± 0.04	1.44 ± 0.04	1.44 ± 0.04	...
ρ_c (g cm^{-3})	$2.31^{+3.54}_{-1.97}$	10.9 ± 2.75	10.4 ± 2.39	...

Note. Planet parameters were derived based on the stellar parameters reported in Fulton & Petigura (2018). We also report the radii of both planets from Fulton & Petigura (2018) to compute their densities, although the planet radii were not directly measured in this paper. It is also worth noting that in TTVFaster, 180° was added to the argument of periastron of the planets (ω_b and ω_c) to address the inconsistency in the modeling of ω between RadVel and TTVFaster.

activity (Rajpaul et al. 2015; Nicholson & Aigrain 2022), we used a quasi-periodic kernel with RadVel:

$$C_{ij} = A^2 \exp \left[-\frac{|t_i - t_j|^2}{\lambda_e^2} - \frac{\sin^2(|t_i - t_j|/P_{\text{rot}})}{2\lambda_p^2} \right]. \quad (3)$$

Here, i and j are indexes of the covariance matrix C and A , λ_e , P_{rot} , and λ_p are the hyperparameters of our quasi-periodic kernel, representing the GP amplitude, the exponential decay timescale (a proxy for the lifetime of star spots), the stellar rotation period, and the harmonic complexity, respectively. While GPs provide the flexibility to fit complex data sets, they are notorious for overfitting. To mitigate this issue, we imposed physically motivated priors on the GP hyperparameters:

$$\begin{aligned} 0 &\leq A \leq \sigma_{\text{RV}} \\ 0.5P_{\text{rot}} &\leq \lambda_e \leq 10P_{\text{rot}} \\ 0 &\leq P_{\text{rot}} \leq 50.5 \text{ days} \\ 0.5 &\leq \lambda_p \leq 5. \end{aligned} \quad (4)$$

For A , this broad prior prevents the overall GP amplitude from exceeding the standard deviation of the RVs. The prior on P_{rot} is set between 0 and the 3σ upper bound reported in McQuillan et al. (2013). For the priors on λ_e and λ_p , we follow the recommendations of Rajpaul (2017).

3.3. Three-planet Models

In addition to the two-planet models described in Sections 3.1 and 3.2, we also ran two different three-planet RV models. For these models, we adopt the same approaches as Section 3.1 (non-GP) and Section 3.2 (GP), with the addition of the third candidate planet. Specifically, we included the $0.55 R_\oplus$ candidate planet at 3.43 days, with a Gaussian prior on P and t_0 based on Thompson et al. (2018).

3.4. Model Comparison

Based on these set-ups, we ran the MCMC code embedded within RadVel for these models to maximize the following

log-likelihood function:

$$\log(\mathcal{L}) = -0.5 \left(\sum_k \frac{(\text{RV}_k - \text{RV}_{m,k}(t_k))^2}{\sigma_{\text{RV},k}^2} + \log(\sigma_{\text{RV},k}^2) \right) \quad (5)$$

where RV_k is the k -th observed RV measurement, and $\text{RV}_{m,k}(t_k)$ is the Keplerian-modeled RV at time t_k . $\sigma_{\text{RV},k}$ is the uncertainty for the k -th RV measurement, which is defined as the observational uncertainty (σ_k) added together in quadrature with a jitter (σ_{jitter}) term: $\sqrt{(\sigma_k)^2 + (\sigma_{\text{jitter}})^2}$. We ran this MCMC algorithm with 50 walkers until convergence. The initial 10% of steps were discarded as burn-in. To check for convergence, we once again required the PSRF to be less than 1.01 for each parameter.

Our two-planet non-GP RadVel fit to the RV data yielded a mass of $10.7 \pm 2.8 M_\oplus$ for Kepler-105b (Figure 2). We were unable to strongly detect Kepler-105c in the RVs, so we only placed a 95% upper limit of $4.6 M_\oplus$ for this planet. In comparison, our two-planet fit with a GP yielded masses of $M_b = 10.2 \pm 2.6 M_\oplus$ and $M_c < 3.8 M_\oplus$ (95% upper limit). Thus, both models produced similar masses for Kepler-105b and Kepler-105c. Given that the results were nearly identical, we determined that the added complexity of a GP is not justified for Kepler-105 since the simpler model is strongly favored ($\Delta\text{AIC} = -32$). Furthermore, the two different three-planet models did not detect the $0.55 R_\oplus$ candidate planet, placing 95% upper limits of 4.6 (non-GP) and $4.8 M_\oplus$ (GP). These models also failed to detect an RV signal for Kepler-105c, only placing 95% upper limits of 4.6 (non-GP) and $4.7 M_\oplus$ (GP). Since these models are strongly disfavored to our two-planet non-GP fit ($\Delta\text{AIC} > 38$ for both models) and no additional planetary signals were detected in the Lomb–Scargle periodogram of the RVs (Lomb 1976; Scargle 1982), we conclude that the simple two-planet model is the best fit to the RVs of Kepler-105.

3.5. Why did not We Detect Kepler-105c in the RVs?

In an effort to understand why Kepler-105c was not detected in the RVs, we conducted an injection-recovery test where we injected a synthetic planetary signal into the RVs based on the

Table 2
Kepler-105 RV Observations and Activity Indicators (HIRES)

BJD	RV (m s ⁻¹)	σ_{RV} (m s ⁻¹)	S_{HK}	σ_{SHK}
2457197.948219	-17.85	3.03	0.146	0.001
2457200.991239	-4.32	2.74	0.1402	0.001
2457202.062219	-5.11	2.57	0.1422	0.001
2457204.037027	2.88	2.83	0.1406	0.001
2457222.06666	-1.24	3.12	0.1384	0.001
2457229.095178	-14.22	3.20	0.1347	0.001
2457229.900375	-6.14	2.94	0.1377	0.001
2457236.943638	18.74	3.43	0.1225	0.001
2457245.979016	-1.00	2.79	0.1357	0.001
2457254.93196	2.63	2.85	0.1338	0.001
2457255.995104	-7.12	3.34	0.1256	0.001
2457262.890422	1.94	2.79	0.1382	0.001
2457265.012706	9.46	3.16	0.1264	0.001
2458627.914381	9.63	2.61	0.1498	0.001
2458679.988635	-5.32	2.33	0.1449	0.001
2458714.842907	6.50	2.43	0.1295	0.001
2458722.907216	-1.66	2.35	0.1288	0.001
2458765.847403	-3.04	2.81	0.1314	0.001
2458776.858662	3.57	3.60	0.1236	0.001
2458795.779808	6.51	2.93	0.1271	0.001
2458999.960787	-9.50	2.91	0.1357	0.001
2459003.060371	-5.21	3.14	0.1347	0.001
2459003.971311	-5.99	2.54	0.1344	0.001
2459006.950713	1.71	2.84	0.138	0.001
2459007.993173	1.57	3.02	0.1358	0.001
2459010.998866	0.85	2.77	0.1375	0.001
2459011.985675	1.31	2.87	0.1374	0.001
2459012.983941	3.27	3.18	0.1363	0.001
2459014.048065	-0.73	2.72	0.134	0.001
2459016.916247	-7.59	3.09	0.1322	0.001
2459024.926903	7.67	2.99	0.1313	0.001
2459028.860562	12.46	2.64	0.1362	0.001
2459030.954948	-3.39	2.98	0.1313	0.001
2459035.972648	-8.55	3.02	0.133	0.001
2459040.000646	1.72	2.72	0.1323	0.001
2459071.053519	-3.92	4.11	0.1172	0.001
2459078.03372	6.28	2.99	0.1297	0.001
2459088.889249	-0.20	3.41	0.114	0.001
2459091.966282	-1.57	3.34	0.1187	0.001
2459101.920248	-0.80	2.94	0.1241	0.001
2459114.882941	5.32	2.90	0.1251	0.001
2459117.819583	6.51	2.86	0.1273	0.001
2459119.838001	-0.91	3.16	0.1221	0.001
2459120.820908	2.31	2.93	0.1258	0.001
2459121.879195	0.25	2.86	0.1224	0.001
2459122.889507	-2.53	2.99	0.1248	0.001
2459123.838387	-0.13	3.20	0.1245	0.001
2459153.804096	7.43	3.34	0.1165	0.001
2459362.071766	-4.08	2.57	0.1505	0.001
2459373.881189	-4.01	2.83	0.1465	0.001
2459376.952544	-2.11	2.94	0.1455	0.001
2459377.907244	-1.74	2.90	0.1439	0.001
2459378.938855	-6.85	2.47	0.1484	0.001
2459379.962735	-5.36	2.67	0.1472	0.001
2459383.035088	-8.71	2.78	0.1404	0.001
2459385.946136	1.06	2.53	0.1446	0.001
2459386.913853	9.81	2.77	0.1459	0.001
2459387.954846	-0.16	3.25	0.1482	0.001
2459388.972634	-0.43	2.75	0.1479	0.001
2459389.978382	-5.01	3.00	0.1461	0.001
2459395.952932	-9.22	2.99	0.1395	0.001
2459399.92468	-9.62	2.87	0.1422	0.001
2459405.02193	-3.94	2.42	0.1408	0.001
2459406.013179	-7.70	2.91	0.1415	0.001

Table 2
(Continued)

BJD	RV (m s ⁻¹)	σ_{RV} (m s ⁻¹)	S_{HK}	σ_{SHK}
2459406.93291	-6.74	2.71	0.1419	0.001
2459409.033993	-5.26	2.76	0.1408	0.001
2459410.042219	-6.46	3.20	0.1403	0.001
2459415.055976	-19.57	3.76	0.1379	0.001
2459422.966883	4.13	3.20	0.1385	0.001
2459435.851129	-0.82	2.62	0.1348	0.001
2459441.002974	-9.05	3.24	0.1315	0.001
2459441.953438	0.62	2.90	0.1377	0.001
2459443.838183	2.39	2.57	0.1351	0.001
2459445.03636	-0.84	2.81	0.1365	0.001
2459445.96299	6.17	3.46	0.1362	0.001
2459448.921949	8.09	2.96	0.1356	0.001
2459449.919675	10.45	2.60	0.1343	0.001
2459450.90239	3.24	2.91	0.1392	0.001
2459451.919987	2.17	3.14	0.1354	0.001
2459452.858454	-5.16	2.59	0.1338	0.001
2459455.849691	5.52	2.53	0.1369	0.001
2459456.959194	8.45	2.93	0.1362	0.001
2459469.823537	12.58	2.70	0.1363	0.001
2459470.831935	-8.23	2.56	0.1369	0.001
2459471.755624	-5.45	2.53	0.137	0.001
2459474.903543	4.31	3.59	0.1331	0.001
2459475.876222	-8.19	3.30	0.1285	0.001
2459482.91076	4.51	3.30	0.132	0.001
2459484.819239	6.21	2.56	0.1373	0.001
2459489.884357	3.00	3.56	0.134	0.001
2459498.826307	5.04	3.21	0.1404	0.001
2459502.881921	5.88	3.09	0.1353	0.001
2459503.837569	-11.50	2.93	0.1359	0.001

Note.

^a A full machine-readable table of the data is available in the online journal and includes additional columns showing UTC time, OBSIDs, raw spectrum counts, χ^2 values, barycentric velocities, and telluric-calibrated radial velocities.

(This table is available in its entirety in machine-readable form.)

posteriors of Kepler-105c from the TTVs. Even with the injected signal, we still do not strongly detect Kepler-105c in the RV data. This is somewhat surprising: Kepler-105c should generate a signal of 2 m s^{-1} based on its TTV mass ($5.9 \pm 1.4 M_{\oplus}$). According to Equation (7) of Howard & Fulton (2016), a 2 m s^{-1} signal is expected to be detectable with 6σ confidence in a sample of 92 RVs. However, it is important to note that the Howard & Fulton (2016) relation is primarily derived from the RVs of giant planets. This could limit its relevance to smaller planets like Kepler-105b and Kepler-105c, which may explain why we only detected the more massive Kepler-105b with 4σ confidence and did not strongly detect Kepler-105c. Other factors, such as the presence of additional planets or unmitigated stellar activity, may also contribute to our failure to confidently detect Kepler-105c in the RVs. Furthermore, discrepancies between RV and TTV mass estimates are not unprecedented and have been a subject of ongoing study for many years (Weiss & Marcy 2014; Steffen 2016; Mills & Mazeh 2017; Otegi et al. 2020). As a result, this discrepancy between the RV- and TTV-determined mass of Kepler-105c merits further scrutiny, both to understand the specific case of Kepler-105c as well as the broader issue of reconciling measured RV and TTV masses.

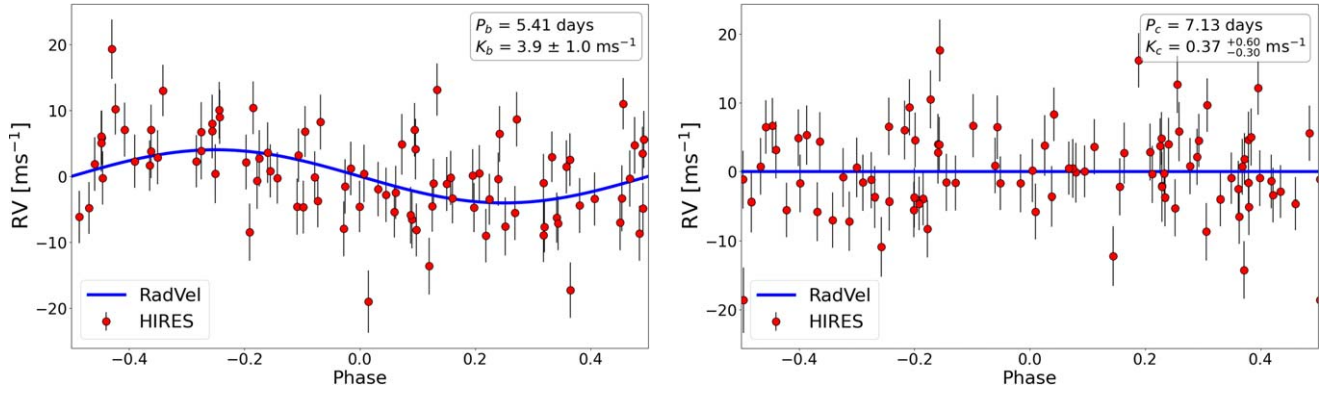


Figure 2. Phase-folded RVs (red) and the `RadVel` (Fulton et al. 2018) fit to the RVs (blue) for Kepler-105b (left) and Kepler-105c (right). The `RadVel` two-planet fit without a GP yielded a 4σ detection of Kepler-105b ($10.7 \pm 2.8 M_{\oplus}$) but did not strongly detect Kepler-105c, despite imposing a planetary signal at its known orbital period. Thus, we can only place a 95% upper limit of $4.6 M_{\oplus}$ on the mass of Kepler-105c based on only the RVs.

4. Joint Modeling of RVs and TTVs

In the previous sections, we analyzed the RVs and TTVs separately. The TTVs placed strong constraints on the mass of Kepler-105c but not Kepler-105b, while the opposite was true for the RVs. To obtain precise mass measurements for both planets, we combined these two methods using a joint RV and TTV model. To do this, we used `TTVFaster` and `RadVel` to maximize the log-likelihood function

$$\log(\mathcal{L}) = -0.5 \left(\sum_i \frac{(\text{TT}_i - \text{TT}_{m,i})^2}{\sigma_{\text{TT},i}^2} + \sum_k \frac{(\text{RV}_k - \text{RV}_{m,k}(t_k))^2}{\sigma_{\text{RV},k}^2} + \log(\sigma_{\text{RV},k}^2) \right). \quad (6)$$

With this setup, we used the python package `emcee` to vary the masses, orbital periods, $\sqrt{e} \cos \omega_*$, $\sqrt{e} \sin \omega_*$, and initial transit times for both planets, as well as the nuisance parameters γ and σ . It is important to note that `TTVFaster` and `RadVel` use different conventions where the ascending node and value of ω_* differ by 180° (Householder & Weiss 2022). Here, we adopt the `RadVel` convention, which uses a \hat{Z} unit vector that points away from the observer and defines the ascending node as the point where the planet pierces the sky plane moving away from the observer. This is opposite to the coordinate system used in `TTVFaster`, where \hat{Z} points toward the observer and the planet approaches the observer at the ascending node. To account for this difference, we added 180° to the value of ω_* in the `TTVFaster` component of our model (note that `TTVFaster` specifically models ω_p , but it is straightforward to convert between ω_p and ω_* : $\omega_* = \omega_p + 180^\circ$). Similarly to our other models, we implemented uniform priors on e , M , ω and Gaussian priors on p and t_0 . We also used a Gaussian prior on stellar mass as well as a Hill stability prior. We ran this MCMC for 8×10^5 steps, discarding the first 10^5 steps as burn-in. To ensure that our chains converged, we required the PSRF to be less than 1.01 for each parameter in our model. All of the chains met this PSRF threshold. This MCMC model yielded masses of $10.8 \pm 2.3 M_{\oplus}$ and $5.6 \pm 1.2 M_{\oplus}$ for Kepler-105b and Kepler-105c, respectively (Table 1).

5. Planet Interiors

Using the radius measurements from Fulton & Petigura (2018), we can now plot Kepler-105b and Kepler-105c on a

mass–radius diagram (Figure 3). While the masses and radii alone cannot reveal the composition of the planets, this figure does provide some insight into their potential compositions. The mass and radius of Kepler-105c are consistent with a rocky planet without a significant gaseous envelope. Kepler-105b, on the other hand, lies above the 100% rocky composition line, suggesting that Kepler-105b has a substantial volatile envelope. Assuming that Kepler-105b has an Earth-like core mass fraction of 67.5% MgSiO_3 and 32.5% Fe (Seager et al. 2007), the envelope mass fraction of H_2 -He of Kepler-105b would be between 0.5% and 2% (Lopez & Fortney 2014).

Another possible composition that has been suggested for planets of similar masses and sizes to Kepler-105b is that of a “water world”: a rocky planet with hundreds or thousands of kilometers of water, although the existence of such planets remains a topic of debate (Bean et al. 2021; Neil et al. 2022; Rogers et al. 2023). If Kepler-105b is a water world, it likely would have formed beyond the H_2O snow line and migrated inward to its present orbit via Type I migration. This scenario is supported by the fact that Kepler-105b and Kepler-105c are near the 4:3 mean-motion resonance, as Type I migration is a common mechanism for the formation of planets in mean-motion resonances (Kley & Nelson 2012). However, this would require Kepler-105c to form beyond the snow line, which is inconsistent with its high density ($\rho_c = 10.4 \pm 2.39 \text{ g cm}^{-3}$). It may have been possible for Kepler-105c to form in situ and for Kepler-105b to migrate from beyond the snow line, but this would necessitate a fast orbit crossing between the planets. Given these challenges, it seems more plausible that Kepler-105b has a H_2 -He dominate envelope rather than being a water world, but it is difficult to make a definitive assertion without better observational evidence. Unfortunately, it will be difficult to determine the precise composition of the atmosphere of Kepler-105b, even with potential follow-up observations. Its atmospheric characterization with the James Webb Space Telescope is not feasible (see Transit Spectroscopy Metric; Kempton et al. 2018), primarily due to the faint magnitude of Kepler-105 ($J \approx 11.8$).

6. Scenarios for Atmospheric Mass Loss

6.1. Photoevaporation

Recently, there has been a growing interest in testing photoevaporation models in systems like Kepler-105 where rocky super-Earths are exterior to gaseous sub-Neptunes

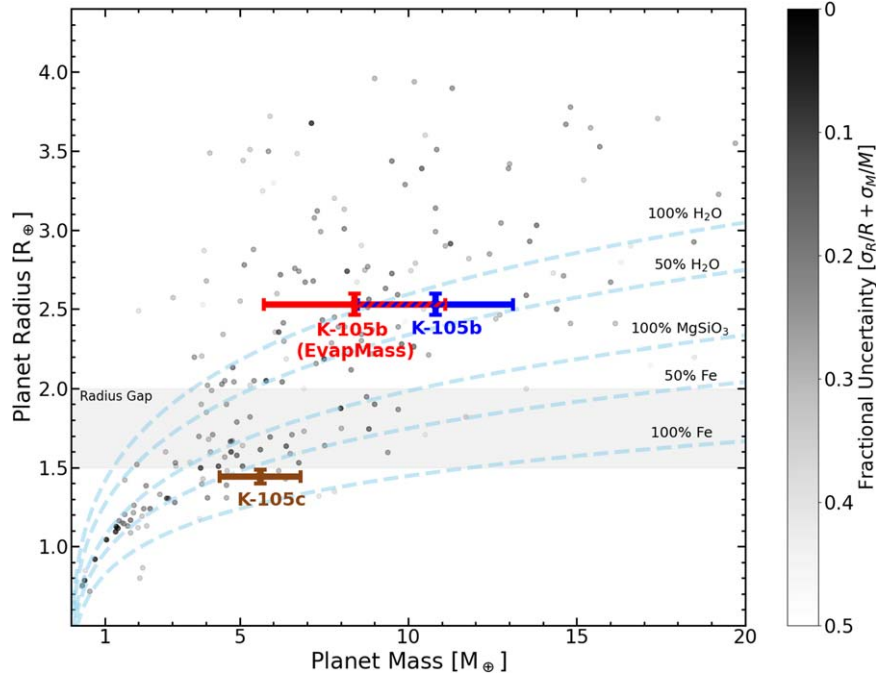


Figure 3. The mass–radius relationship for transiting exoplanets with combined fractional mass and radius uncertainties less than 50% (plotted in gray as a function of fractional uncertainty), based on the NASA Exoplanet Archive (Akeson et al. 2013; queried on 2022 September 22). We also depict the radius gap (Fulton et al. 2017) from $1.5 R_{\oplus}$ to $2.0 R_{\oplus}$ (light gray) as well as the planetary compositions (light blue, dashed) from Zeng et al. (2019). Additionally, we include the 1σ radius (Fulton & Petigura 2018) and mass measurements of Kepler-105b (blue, $2.53 \pm 0.07 R_{\oplus}$, $10.8 \pm 2.3 M_{\oplus}$) and Kepler-105c (brown, $1.44 \pm 0.04 R_{\oplus}$, $5.6 \pm 1.2 M_{\oplus}$). We also show the `EvapMass` (Owen & Campos Estrada 2020b) predicted 1σ minimum mass distribution for Kepler-105b that is consistent with photoevaporation (red, $8.7 \pm 2.4 M_{\oplus}$). If the measured mass of Kepler-105b is greater than the `EvapMass` prediction, then the difference in gas content between Kepler-105b and Kepler-105c can be explained by photoevaporation. Comparing these distributions, we conclude that the difference in gas envelopes of the Kepler-105 planets is entirely attributable to photoevaporation in 76% of scenarios (i.e., $M_{p,\text{measured}} > M_{p,\text{predicted}}$).

(Owen & Campos Estrada 2020a). Such planetary architectures offer a unique testbed for photoevaporation because the sub-Neptune retained its gaseous envelope despite being subject to more cumulative XUV flux (assuming in situ formation). With the masses from our joint RV and TTV analysis, we can assess if the Kepler-105 planets have a formation history that is consistent with photoevaporation. In this context, “consistent with photoevaporation” means that the measured masses and radii of the Kepler-105 planets support the hypothesis that Kepler-105c lost its gaseous envelope due to photoevaporation, while Kepler-105b retained a significant gaseous envelope. To evaluate the validity of this hypothesis, we used the publicly available code `EvapMass` (Owen & Campos Estrada 2020b).

We provide a brief outline of the `EvapMass` numerical procedure, which is more fully described in Owen & Campos Estrada (2020a). `EvapMass` assumes that both Kepler-105b and Kepler-105c formed in situ with H_2 –He envelopes and that Kepler-105c was *just* able to lose its envelope entirely due to photoevaporation, maximizing its atmospheric mass-loss timescale. The atmospheric loss timescale, t_m , is given by $t_m = M_{\text{env}}/\dot{M}_{\text{env}}$ where the equation for the rate of atmospheric mass loss (\dot{M}_{env}) is expressed as follows (Owen & Campos Estrada 2020a):

$$\dot{M}_{\text{env}} = \frac{\eta L_{\text{XUV}} R_p^3}{4GM_p a_p^2}. \quad (7)$$

The variables η , L_{XUV} , and G , represent the mass-loss efficiency, XUV luminosity of the host star, and the gravitational constant, respectively. Since the Kepler-105 planets have $\sim 99\%$ of their mass in solid materials (Section 4), we can assume that

$M_p \approx M_{\text{core}}$, so the equation for t_m can be written as:

$$t_m = \frac{4GM_p^2 a_p^2 X}{\eta L_{\text{XUV}} R_p^3} \quad (8)$$

where X is the envelope mass fraction: $X \equiv M_{\text{env}}/M_{\text{core}}$. For Kepler-105c, our goal is to find the envelope mass at which the mass-loss timescale is maximized. Since we assumed that Kepler-105c formed in situ and that $M_p \approx M_{\text{core}}$, L_{XUV} , M_p , and a_p are independent of the envelope mass. Thus, we can maximize the following:

$$t_m \propto \frac{X}{\eta R_p^3}. \quad (9)$$

`EvapMass` solves for these dependencies numerically (i.e., computing X as a function of M , a , and R involves numerically evaluating several integrals) and then compares the mass-loss timescales for the two planets (Owen & Campos Estrada 2020a). Since Kepler-105b has a significant gaseous envelope, we require that its atmospheric mass-loss timescale is greater than or equal to the maximum atmospheric mass-loss timescale of the rocky Kepler-105c. This approach effectively minimizes the mass-loss timescale for Kepler-105b, providing us with a mass lower limit for Kepler-105b that is consistent with photoevaporation. If Kepler-105b had a mass below this value, its mass-loss timescale would be too short to sustain its current gaseous envelope, given that Kepler-105c was stripped of its envelope due to photoevaporation.

`EvapMass` was specifically designed to compute a minimum mass without measured masses and is often used to report a 95% limit that the planet mass must be bigger than to be

consistent with photoevaporation (Owen & Campos Estrada 2020a). However, with the availability of our measured posterior distributions of the Kepler-105 planets, we can adopt a slightly different approach. By randomly selecting samples from these posterior distributions, `EvapMass` can compute a minimum mass for each sample. We can compare each minimum mass with the corresponding measured mass to determine the percentage of samples where the measured mass of Kepler-105b is greater than its `EvapMass` predicted minimum mass. A higher percentage of cases where the measured mass is greater the `EvapMass` predicted minimum mass indicates a higher consistency with photoevaporation.

Since the `EvapMass` computation depends on both the mass and radius of Kepler-105b and Kepler-105c as well as the properties of their host star (i.e., temperature, mass, radius, age), we evaluated 50,000 randomly drawn samples from these measured distributions. We adopted a value of $1.8 R_{\oplus}$ for the location of the radius gap, a value that is generally accepted for FGK stars, although it can be lower ($\sim 1.5 R_{\oplus}$) for M-dwarfs (Van Eylen et al. 2018, 2021). This selection means that the entire radius distribution of Kepler-105c falls below the radius gap. Our calculations for η are based on the hydrodynamical models from Owen & Jackson (2012). Using Fulton & Petigura (2018) for our host-star properties and planet radii, combined with our measured mass distribution of Kepler-105c, we computed a minimum mass distribution of $8.7 \pm 2.4 M_{\oplus}$ for Kepler-105b, assuming Kepler-105c was stripped of its envelope due to photoevaporation (Figure 3). For each of our 50,000 samples, we compared the measured mass sample of Kepler-105b with the predicted mass sample of Kepler-105b using `EvapMass`. Our analysis revealed that 76% of the compared samples were consistent with photoevaporation (i.e., $M_{b,\text{measured}} > M_{b,\text{predicted}}$). Thus, we conclude that it is probable that the difference in gas content of the Kepler-105 planets is consistent with a history of photoevaporation.

For the 24% of cases that are inconsistent with photoevaporation (i.e., $M_{b,\text{measured}} < M_{b,\text{predicted}}$), we find that these scenarios are also inconsistent with core-powered mass loss in 99% of cases (details of this procedure can be found in Section 6.2). In these scenarios, stochastic events such as giant impacts (Inamdar & Schlichting 2015; Bonomo et al. 2019) could explain the differing envelope fractions of the planets. It is also possible that the Kepler-105 planets underwent migration, in which case their present gas envelopes need not be consistent with in situ mass-loss predictions.

6.2. Core-powered Mass Loss

Since we tested the viability of photoevaporation to explain the difference in gas content between Kepler-105b and Kepler-105c, it is natural to explore another frequently cited mechanism for the radius gap: core-powered mass loss. Core-powered mass loss relies on the internal heat from a planet's core and the thermal radiation from the host star to drive the evaporation of its atmosphere (Ginzburg et al. 2018). Rather than conduct a full numerical procedure like we did for photoevaporation, we follow the simpler approach of Cloutier et al. (2020). Specifically, we required the timescale for core-powered atmospheric mass loss for Kepler-105b to be greater than or equal to that of Kepler-105c. This condition provides the following constraint on planetary parameters (derived in

Appendix B of Cloutier et al. 2020):

$$1 \leq \left(\frac{M_{\text{core},b}}{M_{\text{core},c}} \right) \left(\frac{T_{\text{eq},b}}{T_{\text{eq},c}} \right)^{-3/2} \times \exp \left[c' \left(\frac{M_{\text{core},b}}{T_{\text{eq},b} R_b} - \frac{M_{\text{core},c}}{T_{\text{eq},c} R_c} \right) \right] \quad (10)$$

where $M_{\text{core}} \approx M_p$, T_{eq} is the equilibrium temperature of the planet and c' is a constant: $\sim 10^4 \text{ K } R_{\odot} M_{\odot}^{-1}$. We use host star properties to compute T_{eq} for both planets:

$$T_{\text{eq}} = T_{\text{eff}} \sqrt{\frac{R_*}{2a}} (1 - A_B)^{1/4} \quad (11)$$

where T_{eff} and R_* are the temperature and radius of the star, and A_B is the Bond albedo. Assuming Gaussian distributions for T_{eff} and R_* ($5933 \pm 60 \text{ K}$, $1.03 \pm 0.02 R_{\odot}$) based on Fulton & Petigura (2018) and choosing a Bond albedo of 0.3 for both planets, we compute $T_{\text{eq},b} = 1076 \pm 15 \text{ K}$ and $T_{\text{eq},c} = 981 \pm 13 \text{ K}$. When we apply Equation (10) to these equilibrium temperatures and the mass and radius distributions of Kepler-105b and Kepler-105c, we find that these planets satisfy the condition for core-powered mass loss (Equation (10)) in 48% of scenarios.

6.3. Varying Bond Albedo

While our analysis suggests that core-powered mass loss is a plausible explanation for the atmospheric differences in the Kepler-105 planets, it is important to consider the role of Bond albedo in our computation. For instance, if we use a Bond albedo for Kepler-105c that is similar to Venus ($A_b = 0.8$) instead of 0.3, $T_{\text{eq},c} = 717 \pm 10 \text{ K}$. With this single alteration, the consistency of these planets with core-powered mass loss decreases from 48% to 12%. Conversely, if we instead change the Bond albedo of Kepler-105b to 0.8, the consistency increases to 86%. Thus, while our analysis suggests that core-powered mass loss could potentially explain the differences in gas content between Kepler-105b and Kepler-105c, better measurements of T_{eq} or A_b will be necessary for a more definitive assessment.

We also explored the implications of varying the Bond albedo on the photoevaporation models in Section 6.1. `EvapMass` assumes a Bond albedo of 0 for both planets when computing their equilibrium temperature. We found that setting both A_b and A_c to 0.3 for the calculation of T_{eq} resulted in 83% consistency with photoevaporation. Altering these values to $A_b = 0.3$, $A_c = 0.8$ and $A_b = 0.8$, $A_c = 0.3$ led to slightly different consistencies of 81% and 93%, respectively. Since the equilibrium temperature is essentially a proxy for stellar flux in `EvapMass`, we can also modify the atmosphere's response by varying the opacity, κ , given by the following:

$$\kappa = \kappa_0 P^{\alpha} T^{\beta}. \quad (12)$$

Here, κ_0 is the opacity constant and α and β describe the pressure (P) and temperature (T) dependence of opacity. By default, `EvapMass` sets $\kappa_0 = 10^{-7.32}$, $\alpha = 0.68$, and $\beta = 0.45$, where pressure and temperature are expressed in cgs units (Rogers & Seager 2010). We varied κ_0 by an order of magnitude (i.e., $\kappa_0 = 10^{-6.32}$, $\kappa_0 = 10^{-8.32}$). For these scenarios, the consistency with the photoevaporation model remained 76%.

Thus, the photoevaporation models are less sensitive to changes in Bond albedo compared to core-powered mass-loss models. This result aligns with findings from Owen & Jackson (2012), which demonstrate that photoevaporation mass-loss rates are not highly sensitive to variations in the underlying planetary atmospheric temperature.

Interestingly, systems like Kepler-105 present an opportunity to indirectly constrain the Bond albedo for sub-Neptunes and super-Earths. By jointly modeling photoevaporation and core-powered mass loss in systems like Kepler-105, it may be possible to identify the range of Bond albedos that would allow Kepler-105b to sustain its envelope given that Kepler-105c lost its envelope. This approach could provide us with some of the first Bond albedo constraints for smaller planets, since Bond albedo can typically only be constrained for larger planets with detectable secondary eclipses.

7. Summary and Discussion

In this paper, we investigated the unusual architecture of the Kepler-105 planetary system, with two planets straddling the exoplanet radius gap in an ideal way for testing photoevaporation. By combining precise radial-velocity measurements from HIRES on Keck I with transit-timing variations acquired from the Kepler Space Telescope during Q1-Q17, we measured masses of $10.8 \pm 2.3 M_{\oplus}$ ($\rho_b = 3.68 \pm 0.84 \text{ g cm}^{-3}$) and $5.6 \pm 1.2 M_{\oplus}$ ($\rho_c = 10.4 \pm 2.39 \text{ g cm}^{-3}$) for Kepler-105b and Kepler-105c, respectively. Our numerical mass predictions with `EvapMass` suggest that in 76% of scenarios, the difference in gas envelope content between Kepler-105b and Kepler-105c can be explained by photoevaporation (i.e., $M_{b,\text{measured}} > M_{b,\text{predicted}}$). However, we acknowledge that alternative mechanisms, such as core-powered mass loss, cannot be definitively ruled out at this stage and warrant further investigation. Furthermore, our mass measurements reveal a $\sim 2\sigma$ mass difference between the cores of Kepler-105b and Kepler-105c. While photoevaporation sculpts the gas envelopes of exoplanets, it does not generate differences in the mass of solid materials, leading to an unresolved question: what mechanism produced the difference in solid mass between Kepler-105b and Kepler-105c? Further investigations into the formation and evolution of Kepler-105b and Kepler-105c will be required to determine the underlying mechanisms responsible for the origin of these planets.

Acknowledgments

We thank the anonymous referee whose insights and suggestions significantly enhanced the quality of this manuscript.

This material is based on work supported by the National Science Foundation REU Program (grant No. 2050527). A.H. thanks Beatriz Campos Estrada, Greg Laughlin, Andrew W. Mayo, and the Astroweiss group for useful conversations and feedback. A.H. also thanks Jason Rowe for generously sharing the transit times used in this paper. We are also grateful to Miki Nakajima for her contributions to the proposal that enabled the acquisition of the RV data presented in this work.

L.M.W. acknowledges support from the NASA-Keck Key Strategic Mission Support program (grant No. 80NSSC19K1475) and the NASA Exoplanet Research Program (grant no. 80NSSC23K0269). R.A.R. is supported by the NSF Graduate Research Fellowship, grant No. DGE 1745301. J.M.A.M. acknowledges support from the National Science Foundation Graduate Research Fellowship Program under grant No. DGE-

1842400 and from NASAS Interdisciplinary Consortia for Astrobiology Research (NNH19ZDA001N-ICAR) under award number 19-ICAR19_2-0041. This work was supported by a NASA Keck PI Data Award, administered by the NASA Exoplanet Science Institute. Data presented herein were obtained at the W. M. Keck Observatory from telescope time allocated to (1) the University of Hawai'i, and (2) the National Aeronautics and Space Administration through the agency's scientific partnership with the California Institute of Technology and the University of California. The Observatory was made possible by the generous financial support of the W. M. Keck Foundation.

The authors also wish to recognize and acknowledge the very significant cultural role and reverence that the summit of Maunakea has always had within the indigenous Hawaiian community. We are most fortunate to have the opportunity to conduct observations from this mountain.

Facilities: Keckler, Keck:I

Software: `RadVel` (Fulton et al. 2018), `TTVFaster` (Agol & Deck 2016), `TTVFast` (Deck et al. 2014), `NumPy` (van der Walt et al. 2011), `Matplotlib` (Hunter 2007), `Pandas` (McKinney 2010).

ORCID iDs

Aaron Householder  <https://orcid.org/0000-0002-5812-3236>
 Lauren M. Weiss  <https://orcid.org/0000-0002-3725-3058>
 James E. Owen  <https://orcid.org/0000-0002-4856-7837>
 Howard Isaacson  <https://orcid.org/0000-0002-0531-1073>
 Andrew W. Howard  <https://orcid.org/0000-0001-8638-0320>
 Daniel Fabrycky  <https://orcid.org/0000-0003-3750-0183>
 Leslie A. Rogers  <https://orcid.org/0000-0003-0638-3455>
 Hilke E. Schlichting  <https://orcid.org/0000-0002-0298-8089>
 Benjamin J. Fulton  <https://orcid.org/0000-0003-3504-5316>
 Erik A. Petigura  <https://orcid.org/0000-0003-0967-2893>
 Steven Giacalone  <https://orcid.org/0000-0002-8965-3969>
 Joseph M. Akana Murphy  <https://orcid.org/0000-0001-8898-8284>
 Corey Beard  <https://orcid.org/0000-0001-7708-2364>
 Ashley Chontos  <https://orcid.org/0000-0003-1125-2564>
 Fei Dai  <https://orcid.org/0000-0002-8958-0683>
 Judah Van Zandt  <https://orcid.org/0000-0002-4290-6826>
 Jack Lubin  <https://orcid.org/0000-0001-8342-7736>
 Malena Rice  <https://orcid.org/0000-0002-7670-670X>
 Alex S. Polanski  <https://orcid.org/0000-0001-7047-8681>
 Paul Dalba  <https://orcid.org/0000-0002-4297-5506>
 Sarah Blunt  <https://orcid.org/0000-0002-3199-2888>
 Emma V. Turtelboom  <https://orcid.org/0000-0002-1845-2617>
 Ryan Rubenzahl  <https://orcid.org/0000-0003-3856-3143>
 Casey Brinkman  <https://orcid.org/0000-0002-4480-310X>

References

- Agol, E., & Deck, K., 2016 `TTVFaster`: First order eccentricity transit timing variations (TTVs), *Astrophysics Source Code Library*, ascl:1604.012
 Akaike, H. 1974, *ITAC*, 19, 716
 Akeson, R. L., Chen, X., Ciardi, D., et al. 2013, *PASP*, 125, 989
 Bean, J. L., Raymond, S. N., & Owen, J. E. 2021, *JGRE*, 126, e06639
 Blunt, S., Carvalho, A., David, T. J., et al. 2023, *AJ*, 166, 62
 Bonomo, A. S., Zeng, L., Damasso, M., et al. 2019, *NatAs*, 3, 416
 Carter, J. A., Agol, E., Chaplin, W. J., et al. 2012, *Sci*, 337, 556
 Cloutier, R., Eastman, J. D., Rodriguez, J. E., et al. 2020, *AJ*, 160, 3
 Deck, K. M., Agol, E., Holman, M. J., & Nesvorný, D. 2014, *ApJ*, 787, 132

- Eastman, J., Gaudi, B. S., & Agol, E. 2013, *PASP*, **125**, 83
- Foreman-Mackey, D., Hogg, D. W., Lang, D., & Goodman, J. 2013, *PASP*, **125**, 306
- Fulton, B. J., & Petigura, E. A. 2018, *AJ*, **156**, 264
- Fulton, B. J., Petigura, E. A., Blunt, S., & Sinukoff, E. 2018, *PASP*, **130**, 044504
- Fulton, B. J., Petigura, E. A., Howard, A. W., et al. 2017, *AJ*, **154**, 109
- Gelman, A., & Rubin, D. B. 1992, *StaSc*, **7**, 457
- Ginzburg, S., Schlichting, H. E., & Sari, R. 2018, *MNRAS*, **476**, 759
- Goodman, J., & Weare, J. 2010, *CAMCS*, **5**, 65
- Grunblatt, S. K., Howard, A. W., & Haywood, R. D. 2015, *ApJ*, **808**, 127
- Gupta, A., & Schlichting, H. E. 2019, *MNRAS*, **487**, 24
- Hadden, S., & Lithwick, Y. 2017, *AJ*, **154**, 5
- Haywood, R. D., Collier Cameron, A., Queloz, D., et al. 2014, *MNRAS*, **443**, 2517
- Householder, A., & Weiss, L. 2022, arXiv:2212.06966
- Howard, A. W., & Fulton, B. J. 2016, *PASP*, **128**, 114401
- Howard, A. W., Johnson, J. A., Marcy, G. W., et al. 2010, *ApJ*, **721**, 1467
- Hunter, J. D. 2007, *CSE*, **9**, 90
- Inamdar, N. K., & Schlichting, H. E. 2015, *MNRAS*, **448**, 1751
- Jontof-Hutter, D., Ford, E. B., Rowe, J. F., et al. 2016, *ApJ*, **820**, 39
- Kempton, E. M. R., Bean, J. L., Louie, D. R., et al. 2018, *PASP*, **130**, 114401
- Kley, W., & Nelson, R. P. 2012, *ARA&A*, **50**, 211
- Lithwick, Y., Xie, J., & Wu, Y. 2012, *ApJ*, **761**, 122
- Lomb, N. R. 1976, *Ap&SS*, **39**, 447
- Lopez, E. D., & Fortney, J. J. 2013, *ApJ*, **776**, 2
- Lopez, E. D., & Fortney, J. J. 2014, *ApJ*, **792**, 1
- McKinney, W. 2010, in Proc. of the 9th Python in Science Conf., ed. S. van der Walt & J. Millman (Austin, TX: SciPy), 51
- McQuillan, A., Mazeh, T., & Aigrain, S. 2013, *ApJL*, **775**, L11
- Mills, S. M., & Mazeh, T. 2017, *ApJL*, **839**, L8
- Mordasini, C. 2020, *A&A*, **638**, A52
- Neil, A. R., Liston, J., & Rogers, L. A. 2022, *ApJ*, **933**, 63
- Nicholson, B. A., & Aigrain, S. 2022, *MNRAS*, **515**, 5251
- Otegi, J. F., Bouchy, F., & Helled, R. 2020, *A&A*, **634**, A43
- Owen, J. E., & Campos Estrada, B. 2020a, *MNRAS*, **491**, 5287
- Owen, J. E., & Campos Estrada, B., 2020b EvapMass: Minimum mass of planets predictor, Astrophysics Source Code Library, ascl:2011.015
- Owen, J. E., & Jackson, A. P. 2012, *MNRAS*, **425**, 2931
- Owen, J. E., & Wu, Y. 2013, *ApJ*, **775**, 105
- Owen, J. E., & Wu, Y. 2017, *ApJ*, **847**, 29
- Rajpaul, V., Aigrain, S., Osborne, M. A., Reece, S., & Roberts, S. 2015, *MNRAS*, **452**, 2269
- Rajpaul, V. M. 2017, PhD Thesis, Univ. Oxford
- Rasmussen, C. E., & Williams, C. K. I. 2006, Gaussian Processes for Machine Learning (Cambridge, MA: MIT Press)
- Rogers, J. G., Schlichting, H. E., & Owen, J. E. 2023, *ApJL*, **947**, L19
- Rogers, L. A. 2015, *ApJ*, **801**, 41
- Rogers, L. A., & Seager, S. 2010, *ApJ*, **712**, 974
- Rowe, J. F., Coughlin, J. L., Antoci, V., et al. 2015, *ApJS*, **217**, 16
- Scargle, J. D. 1982, *ApJ*, **263**, 835
- Seager, S., Kuchner, M., Hier-Majumder, C. A., & Militzer, B. 2007, *ApJ*, **669**, 1279
- Steffen, J. H. 2016, *MNRAS*, **457**, 4384
- Thompson, S. E., Coughlin, J. L., Hoffman, K., et al. 2018, *ApJS*, **235**, 38
- van der Walt, S., Colbert, S. C., & Varoquaux, G. 2011, *CSE*, **13**, 22
- Van Eylen, V., Agentoft, C., Lundkvist, M. S., et al. 2018, *MNRAS*, **479**, 4786
- Van Eylen, V., Astudillo-Defru, N., Bonfils, X., et al. 2021, *MNRAS*, **507**, 2154
- Vogt, S. S., Allen, S. L., Bigelow, B. C., et al. 1994, Proc. SPIE, **2198**, 362
- Weiss, L. M., & Marcy, G. W. 2014, *ApJL*, **783**, L6
- Zeng, L., Jacobsen, S. B., Sasselov, D. D., et al. 2019, *PNAS*, **116**, 9723